Inorganic Chemistry

Article

pubs.acs.org/IC

# Thermoelectric Performance Enhancement of Calcium Cobaltite through Barium Grain Boundary Segregation

Paulo Carvillo,[†] Yun Chen,[†] Cullen Boyle,[†] Paul N. Barnes,[‡] and Xueyan Song*[,†]

[†]Department of Mechanical and Aerospace Engineering, West Virginia University, Evansdale Drive, Morgantown, West Virginia 26506, United States

[‡]Army Research Laboratory, 2800 Powder Mill Road, Adelphi, Maryland 20783, United States

**ABSTRACT:** We report the dramatic increase of the Seebeck coefficient $S$ and thermoelectric performance of calcium cobaltite $Ca_3Co_4O_{9+\delta}$ ceramics through non-stoichiometric addition of minute amount of Ba. The nominal chemistry of polycrystal pellets are $Ca_3Ba_xCo_4O_{9+\delta}$ ($x$ = 0, 0.01, 0.05, and 0.1). At 323 K, $S$ of $Ca_3Co_4O_{9+\delta}$ is 135 $\mu$V K$^{-1}$, whereas $S$ of Ba incorporated $Ca_3Ba_{0.05}Co_4O_{9+\delta}$ is 162.5 $\mu$V·K$^{-1}$, which is the highest $S$ value near room temperature regime reported for calcium cobaltite. The increase of $S$ for $Ca_3Ba_{0.05}Co_4O_{9+\delta}$ sample is accompanied by the decrease of the electrical resistivity $\rho$, resulting in high power factor $S^2/\rho$ of 843 $\mu$W·m$^{-1}$ K$^{-2}$ at 1007 K. Moreover, the thermal conductivities $\kappa$ of $Ca_3Ba_xCo_4O_{9+\delta}$ decrease with the increase of the Ba addition. The figure-of-merit $ZT$ for $Ca_3Ba_{0.05}Co_4O_{9+\delta}$ reaches 0.52 at 1073 K and a factor of 2.5 increment in comparison with undoped $Ca_3Co_4O_{9+\delta}$. Nanostructure examinations show that the added Ba segregated at the $Ca_3Co_4O_{9+\delta}$ grain boundaries, while the $Ca_3Co_4O_{9+\delta}$ grain interior is free of Ba. Performance enhancement is attributed to the carrier filtering effect caused by the Ba segregation. In addition, Ba segregation promotes the better crystal alignment and the development of crystal texture.

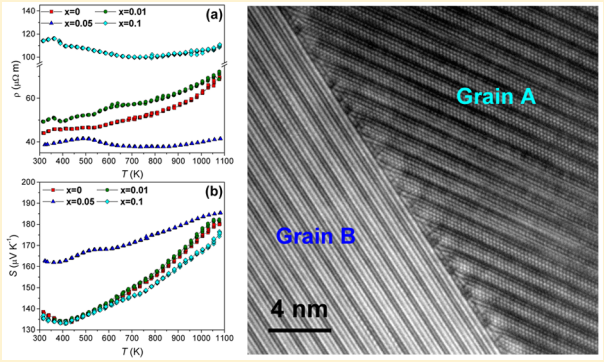


## INTRODUCTION

Thermoelectric (TE) is promising alternative energy conversion technology that converts waste heat from many energy production and consumption systems directly into electricity.[1,2] To achieve a high efficiency in a TE power generator, particularly for high-temperature applications, identifying high-performance TE materials is the key. Misfit layered calcium cobaltite $Ca_3Co_4O_{9+\delta}$ is one of the best p-type TE oxides[3−11] in comparison with other promising oxides. For instance, BiCuSeO system has recently acquired ever-increasing attention in recent years, with dimensionless figure-of-merit $ZT$ increased from 0.5 to 1.4 from year 2010 to year 2014.[12] However, the thermal and chemical stabilities of BiCuSeO are a big concern. BiCuSeO-based materials are stable in air only at temperatures below 573 K, while surface oxidation occurs above 573 K and decomposition becomes apparent at 773 K.[13] In contrast, calcium cobaltite attracts much attentions due to its lightweight, low cost, nontoxicity, and high stability in air at elevated temperatures.[6] The calcium cobaltite single crystal shows good TE behavior with an extrapolated $ZT$ of 0.8 at 973 K.[2] A challenge for developing oxide TE material is to improve the conversion efficiency of polycrystal calcium cobaltite, which is currently low.[3]

One of the approaches that has been successfully introduced to enhance the TE performance of calcium cobaltite is through doping alkaline metals, alkaline earth metals, transition metals, post-transition metals, and/or rare-earth metals at the Ca site and/or Co site.[3,4,8,14−20] For example, a substantial enhancement of electrical transport properties was reached through Yb doping of the Ca site in the $Ca_3Co_4O_{9+\delta}$ system.[8,21,22] Yb doping affects both Seebeck coefficient $S$ and electrical resistivity $\rho$, and the optimum doping level is strongly correlated with the nanostructure, controlled by the pressure of cold pressing.[21] In addition, metallic nanoinclusion such as Ag can also enhance TE properties in both $\rho$ and $S$.[9]

In this paper, we report a novel approach of increasing the TE performance by the non-stoichiometric addition of group 2 heavy metal Ba to polycrystal $Ca_3Co_4O_{9+\delta}$. The nominal chemistry of the modified $Ca_3Co_4O_{9+\delta}$ are $Ca_3Ba_xCo_4O_{9+\delta}$ ($x$ = 0, 0.01, 0.05, and 0.1). The effect of minute amounts of heavy metal Ba nonstoichiometric addition on the performance and nanostructure of bulk $Ca_3Co_4O_{9+\delta}$ was investigated. Particularly, the significant increase of $S$ associated with the Ba segregation at the grain boundaries for $Ca_3Co_4O_{9+\delta}$ ceramic is discussed.

## EXPERIMENTAL SECTION

The precursor powders with the nominal composition of $Ca_3Ba_xCo_4O_{9+\delta}$ ($x$ = 0, 0.01, 0.05, and 0.1) were prepared by a sol−gel chemical solution route. Citric acid (BDH Chemical), ethylene glycol (BDH Chemical), and nominal amounts of $Ca(NO_3)_2{\cdot}4H_2O$ (99%, Acros Organics), $Co(NO_3)_2{\cdot}6H_2O$ (99%, Acros Organics), and

**Received:** June 9, 2015
**Published:** September 11, 2015

ACS Publications © 2015 American Chemical Society



DOI: 10.1021/acs.inorgchem.5b01296
*Inorg. Chem.* 2015, 54, 9027−9032

$Ba(NO_3)_2$ (99.5%, Strem Chemical) were dissolved in deionized water with stirring at 353 K for 3 h to form the gel. The gel was ashed at 773 K in a box furnace. The ashed product was ground using mechanical ball-milling and then calcined at 973 K in a tube furnace with oxygen flow for 4 h to form the precursor powders. The powders were then uniaxially pressed into pellets under 1 GPa at room temperature. The pellets were sintered at 1233 K in a tube furnace with oxygen flow for 9 h to obtain the bulk samples. The absolute Seebeck coefficient $S$ and electrical resistivity $\rho$ were measured in the direction parallel to the pressed plane from 320 K to 1080 K using a Linseis LSR-1100 in a He environment. The thermal conductivities $\kappa$ were measured from 323 to 1073 K in low air pressure using a Laser Flash Analyzer Linseis-1200. The measurement of $\kappa$ was conducted in the direction parallel to the pressed plane of the pellets. X-ray diffraction (XRD) analysis was performed using a PANalytical X'Pert Pro X-ray Diffractometer for phase identification. A JEOL JSM 7600F scanning electron microscope (SEM) and a JEM-2100 transmission electron microscope (TEM) equipped with energy dispersive X-ray spectroscopy (EDS) were used to examine the structure and chemistry from micron to atomic scale. EDS data were taken under TEM with the electron beam diameter set at ~20 nm.

## RESULTS AND DISCUSSION

Table 1 shows the apparent densities for all sample pellets. Among the samples with different Ba addition, the $Ca_3Ba_{0.05}Co_4O_{9+\delta}$ is with the highest mass density. Compared with 4.68 $g\cdot cm^{-3}$ of the calculated density from single-crystal $Ca_3Co_4O_{9+\delta}$,[1] the relative packing densities are 85% and 93% for the undoped and the $Ca_3Ba_{0.05}Co_4O_{9+\delta}$ polycrystal samples, respectively.

**Table 1. Apparent Densities of the Samples $Ca_3Ba_xCo_4O_{9+\delta}$ ($x$ = 0, 0.01, 0.05, and 0.1)**

| $Ca_3Ba_xCo_4O_{9+\delta}$ | apparent density ($g/cm^3$) | relative density (%) |
|---|---|---|
| $x$ = 0 | 3.96 | 85 |
| $x$ = 0.01 | 3.91 | 84 |
| $x$ = 0.05 | 4.33 | 93 |
| $x$ = 0.1 | 3.67 | 78 |

Figure 1a–c shows the temperature dependence of the electrical resistivity $\rho$, Seebeck coefficient $S$, and power factor $S^2/\rho$ for the bulk samples with different Ba addition levels. $\rho$ and $S$ of the $Ca_3Ba_{0.01}Co_4O_{9+\delta}$ sample are comparable to those of the undoped $Ca_3Co_4O_{9+\delta}$ sample, and both increase as temperature increases. Among the Ba added samples, the $Ca_3Ba_{0.05}Co_4O_{9+\delta}$ sample shows overall lowest $\rho$ in the range from 320 to 1080 K. Moreover, $Ca_3Ba_{0.05}Co_4O_{9+\delta}$ exhibits gradually metal–semiconductor transition around 473 K, leading to significantly lower $\rho$ values at higher temperatures and only ~40 $\mu\Omega\cdot$m at 1083 K. In addition, $S$ increases from 138 $\mu V\cdot K^{-1}$ for undoped $Ca_3Co_4O_{9+\delta}$ to 162.5 $\mu V\cdot K^{-1}$ at 400 K for $Ca_3Ba_{0.05}Co_4O_{9+\delta}$, implying the significant decrease of carrier concentrations. Benefiting from both the increased $S$ and decreased $\rho$, $Ca_3Ba_{0.05}Co_4O_{9+\delta}$ reaches the highest power factor $S^2/\rho$ of 843 $\mu W\cdot m^{-1}$ $K^{-2}$ at 1007 K and a factor of 1.7 higher than the undoped sample (peak $S^2/\rho$ of 491 $\mu W\cdot m^{-1}$ $K^{-2}$ at 1005 K). By contrast, much higher $\rho$ and lower $S$ values were observed in $Ca_3Ba_{0.1}Co_4O_{9+\delta}$, which could be attributed to overadding of Ba amount.

The plots of the thermal conductivity $\kappa$ as a function of temperature for different Ba-doped $Ca_3Co_4O_{9+\delta}$ samples are shown in Figure 2a. $\kappa$ decreases as temperature increases, and it decreases with the increase of the Ba amounts. To roughly evaluate the contribution of the electronic thermal conductivity ($\kappa_{el}$) and lattice thermal conductivity ($\kappa_{ph}$) to the total $\kappa$, the

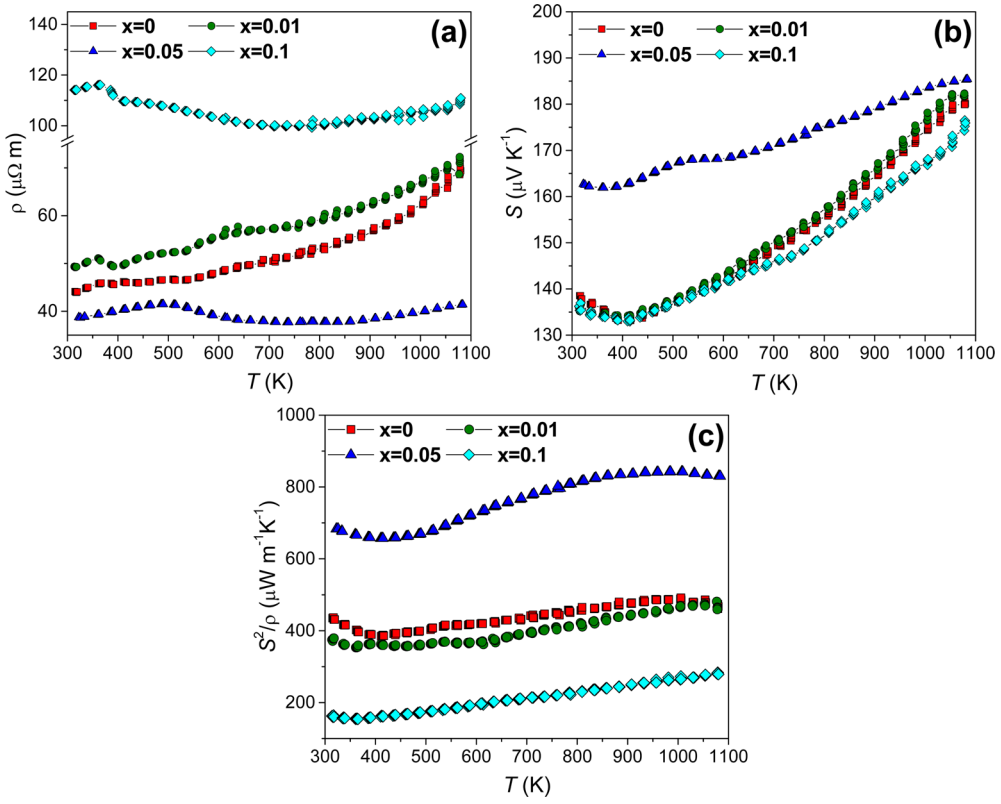


**Figure 1.** Plots of electrical properties for the $Ca_3Ba_xCo_4O_{9+\delta}$ ($x$ = 0, 0.01, 0.05, and 0.1) samples. (a) Electrical resistivity $\rho$ as a function of temperature $T$; (b) Seebeck coefficient $S$ as a function of temperature $T$; and (c) power factor $S^2/\rho$ as a function of temperature $T$.



DOI: 10.1021/acs.inorgchem.5b01296
Inorg. Chem. 2015, 54, 9027–9032

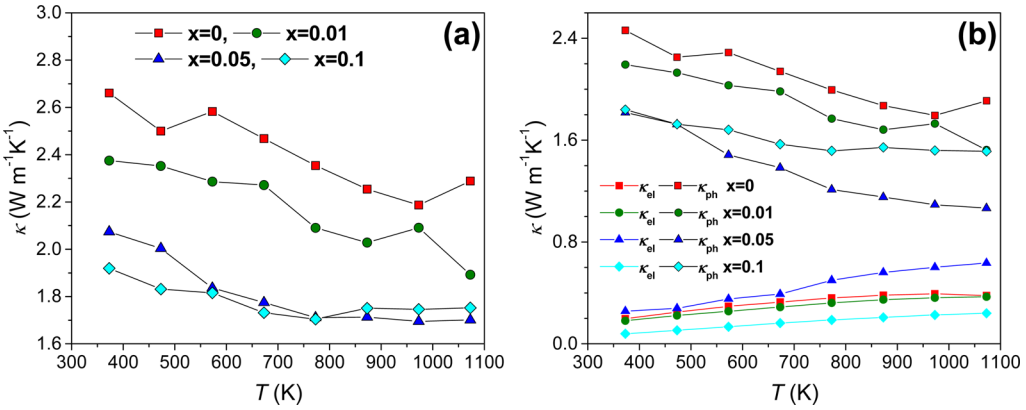


**Figure 2.** (a) Temperature dependence of the thermal conductivity $\kappa$ for the $Ca_3Ba_xCo_4O_{9+\delta}$ ($x$ = 0, 0.01, 0.05, and 0.1) samples. (b) Electronic thermal conductivity ($\kappa_{el}$) and lattice (phonon) thermal conductivity ($\kappa_{ph}$) of total $\kappa$ for $Ca_3Ba_xCo_4O_{9+\delta}$ are estimated by Wiedemann–Franz law ($\kappa_{el} = L_0T/\rho$), where $L_0 = 2.44 \times 10^{-8}$ $V^2$ $K^{-2}$ is Lorentz number based on free-electron model.

Wiedemann–Franz law ($\kappa_{el} = L_0T/\rho$) was applied. Temperature dependences of electron term $\kappa_{el}$ and phonon term $\kappa_{ph}$ were then plotted (in Figure 2b). It is seen that $\kappa_{ph}$ is the predominant component in $\kappa$, and adding Ba reduces $\kappa_{ph}$ of the samples. For $Ca_3Ba_{0.05}Co_4O_{9+\delta}$, phonon scattering effect seems to be remarkably strengthened particularly in higher temperature range though contribution of electron component to total $\kappa$ increased as well.

Dimensionless figure-of-merit $ZT$ is calculated using the equation $ZT = S^2T/\rho\kappa$. The plots of $ZT$ as a function of temperature are shown in Figure 3. The highest $ZT$ values of

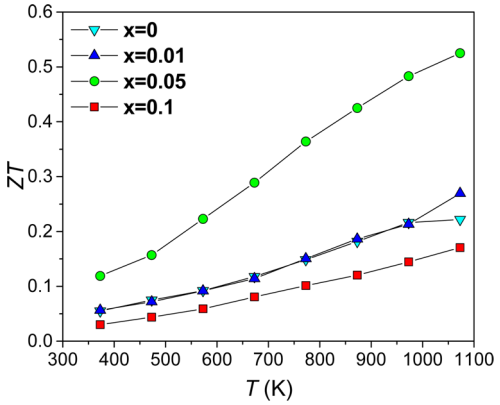


**Figure 3.** Dimensionless figure-of-merit $ZT$ as a function of temperature $T$ for the $Ca_3Ba_xCo_4O_{9+\delta}$ ($x$ = 0, 0.01, 0.05, and 0.1) samples.

0.21 and 0.52 are obtained for the undoped $Ca_3Co_4O_{9+\delta}$ and the $Ca_3Ba_{0.05}Co_4O_{9+\delta}$ sample, respectively. 0.52 at 1023 K is the highest $ZT$ value reported in the polycrystalline $Ca_3Co_4O_9$-based system synthesized using conventional processing. The value approaches the highest reported value of 0.61 for the $Ca_3Co_4O_9$ doped with Ag and Lu and processed using spark plasma sintering instead.[9]

X-ray powder diffraction patterns shown in Figure 4 indicate that all the diffraction peaks can be indexed as those from $Ca_3Co_4O_9$ phase (JCPDS card, No. 23–110). No secondary phase was found, even in the sample with Ba addition of up to 0.1. Also, no peak shifting was observed for all Ba added samples, indicating the $Ca_3Co_4O_9$ lattice parameters are

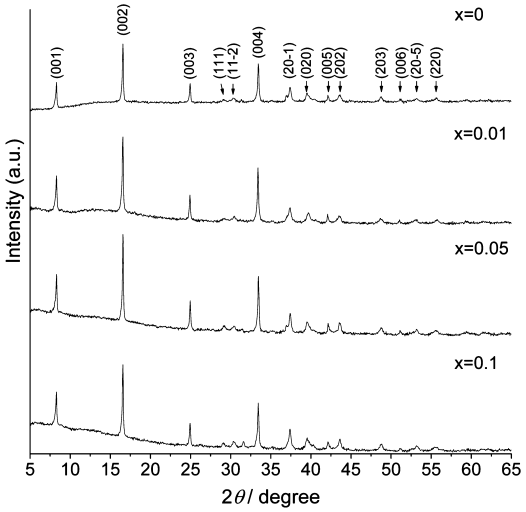


**Figure 4.** XRD powder diffraction patterns for the $Ca_3Ba_xCo_4O_{9+\delta}$ ($x$ = 0, 0.01, 0.05, and 0.1) samples. All the diffraction peaks can be indexed as those from $Ca_3Co_4O_9$ phase (JCPDS card, No. 23–110). No secondary phase was found, and no peak shifting was observed.

unchanged after Ba addition and that Ba probably does not incorporate into the $Ca_3Co_4O_9$ lattice.

The cross-sectional SEM images in Figure 5 from the fractured surface of the pellets clearly show that the plate shape grain alignment and the $c$-axis crystal texture[23] were enhanced with the increase of the Ba addition up to 0.05, while they deteriorate as the Ba concentration further increase to 0.1.

The sample $Ca_3Ba_{0.05}Co_4O_{9+\delta}$ with superior TE performance was subject to TEM examination. The TEM image of Figure 6a depicts the representative intragranular nanolamella structure of $Ca_3Ba_{0.05}Co_4O_9$. The detailed grain boundary nanostructure of $Ca_3Ba_{0.05}Co_4O_9$ is presented in a high-resolution TEM image in Figure 6b. EDS spot examinations were conducted along/near the grain boundary (in Figure 6a), and the results were summarized in Table 2. The EDS examinations indicate that the $Ca_3Co_4O_9$ interior grains are free of Ba. Instead, there is significant Ba segregation occurred at the grain boundaries in between the grains with different $c$-axis orientation.

The Ba segregation at grain boundaries could be explained in term of the size effect or the mismatch of the ionic radius from different cations. The $Ba^{2+}$ is with ionic radius of 149 pm and significantly larger than those from $Ca^{2+}$ of 114 pm and $Co^{2+}$/



DOI: 10.1021/acs.inorgchem.5b01296
Inorg. Chem. 2015, 54, 9027–9032

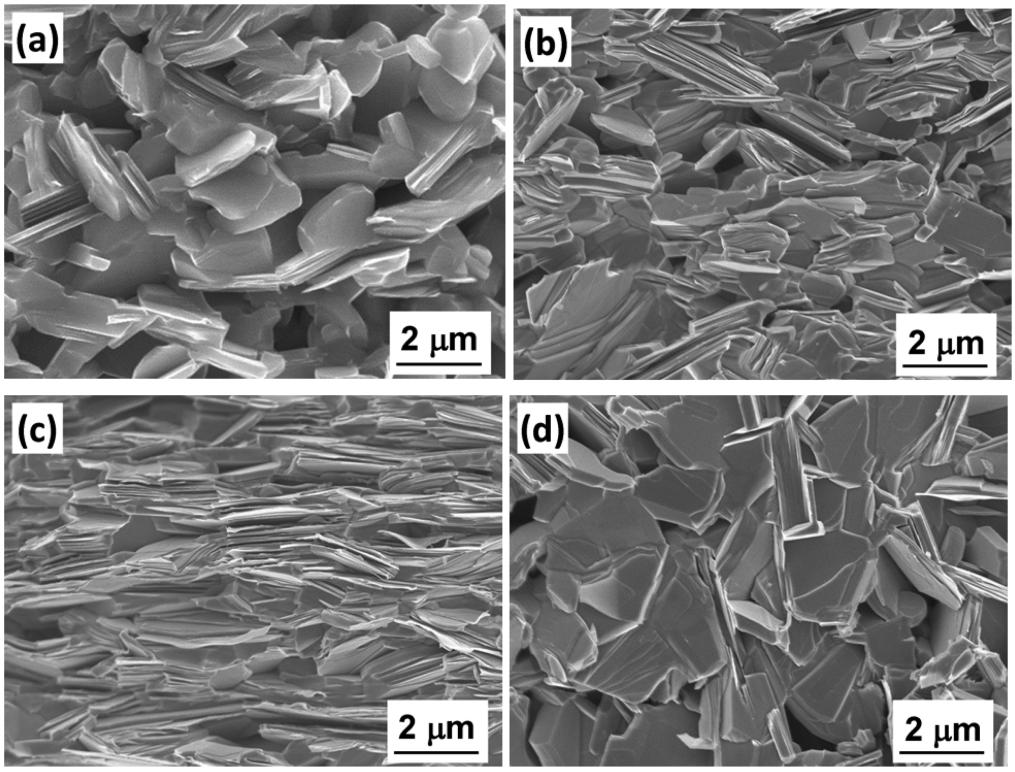


**Figure 5.** Cross-sectional SEM images from the fractured surface of the pellets showing crystal texture of the samples with different Ba concentrations. (a) $Ca_3Co_4O_{9+\delta}$. (b) $Ca_3Ba_{0.01}Co_4O_{9+\delta}$. (c) $Ca_3Ba_{0.05}Co_4O_{9+\delta}$. (d) $Ca_3Ba_{0.1}Co_4O_{9+\delta}$.

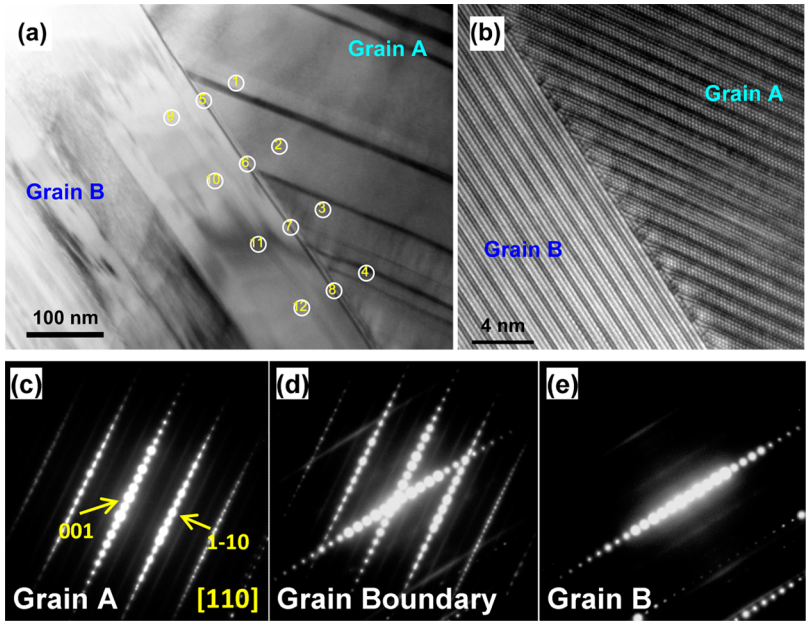


**Figure 6.** Diffraction contrast images and the selected area diffraction patterns from the $Ca_3Ba_{0.05}Co_4O_{9+\delta}$ samples. (a) Low-magnification TEM image showing two $Ca_3Co_4O_{9+\delta}$ grains A and B. The circled numbers (1−12) depict the spots where the EDS spectra were taken from. (b) High-resolution TEM image showing the $Ca_3Co_4O_{9+\delta}$ grain boundary is free of secondary phase. (c) The electron diffraction pattern collected only from grain A. (d) The electron diffraction pattern collected from grain boundary area between grains A and B, and (e) the electron diffraction pattern collected only from grain B.

$Co^{3+}$ of ∼80 pm. The sufficiently larger size of $Ba^{2+}$ prevents itself from being incorporated at a regular atomic site in the $Ca_3Co_4O_9$ lattice. By contrast, $Ca_3Co_4O_9$ grain boundaries in between the lamellas, having different *c*-axis and with low symmetry, are preferred sites for $Ba^{2+}$ to segregate. Furthermore, the Ba grain boundary segregation does not promote the formation of the secondary phase. This finding is supported by both the high-resolution TEM in Figure 6b and the electron diffraction studies as shown in Figure 6c−e. The diffraction patterns of Figure 6c−e were taken from grain A, grain boundary region between grains A and B, and grain B, respectively. The pattern in Figure 6d could be simply



DOI: 10.1021/acs.inorgchem.5b01296
*Inorg. Chem.* 2015, 54, 9027−9032

Table 2. Chemical Compositions of Two Neighboring Grains A (spots 1, 2, 3, and 4) and B (spots 9, 10, 11, and 12) and in between Grain Boundary Area (spots 5, 6, 7, and 8) as Shown in Figure 6a[a]

| atom % | 1 | 2 | 3 | 4 | 5 | 6 | 7 | 8 | 9 | 10 | 11 | 12 |
|---|---|---|---|---|---|---|---|---|---|---|---|---|
| O K | 59.53 | 56.92 | 61.78 | 67.8 | 62.48 | 61.64 | 61.26 | 58.52 | 63.34 | 61.06 | 59.85 | 57.99 |
| Ca K | 17.54 | 20.57 | 17.29 | 13.74 | 15.7 | 16.31 | 16.86 | 18.55 | 16.08 | 17.3 | 17.74 | 18.63 |
| Co K | 22.93 | 22.51 | 20.93 | 18.46 | 21.42 | 21.75 | 21.73 | 22.64 | 20.59 | 21.64 | 22.41 | 23.38 |
| Ba L | 0 | 0 | 0 | 0 | 0.4 | 0.3 | 0.15 | 0.29 | 0 | 0 | 0 | 0 |

[a]The white circles in Figure 6 indicate approximately beam size and each spot location for TEM/EDS spectra collection.

reproduced by superimposing the electron diffraction patterns from the neighboring crystal grains A (in Figure 6c) and B (in Figure 6e), suggesting there are no additional diffraction spots from the secondary phase forming at the grain boundaries.

Remarkably, such Ba grain boundary segregation significantly increases $S$, which implies the decrease of the carrier concentration of the bulk material. In the semiconductor superlattices, it is demonstrated that the electron/carrier filtering not only could be employed as one of the techniques to increase Seebeck coefficient $S$ and the TE power factor $S^2/\rho$ but also resulted in the higher $S^2/\rho$ from heterostructured superlattices in comparison with that from the bulk materials.[24] In the present study, the Ba grain boundary segregation effect associated with the increased $S$ is fully consistent with this discovery on the superlattices of semiconductors. Our hypothesis is that segregation of Ba creates a Ba-enriched barrier layer at $Ca_3Co_4O_9$ grain boundaries. Once it becomes sufficiently thick, such a Ba-enriched barrier layer could impact the intergranular carrier motion and carrier transport. The carrier motion across the Ba-enriched grain boundaries may be limited to those carriers with only sufficiently higher energy. Thus, such filtering effect results in only partial carriers contribute to the conduction, leading to reduced carrier concentration as well as increased $S$.

However, the sample $Ca_3Ba_{0.05}Co_4O_{9+\delta}$ also exhibits significant low $\rho$ in comparison with the undoped sample. Since electrical conductivity $\sigma$ satisfies $\sigma = ne\mu_e$, where $n$ is the number density of electrons and $\mu_e$ is electron mobility, the simultaneous increase of $S$ and decrease of $\rho$ can only result from substantially enhanced bulk carrier mobility. One of the major explanations for the increased carrier mobility is that the doped sample $Ca_3Ba_{0.05}Co_4O_{9+\delta}$ achieved the highly textured microstructure, as evidenced in the SEM image in Figure 5c. Such crystal alignment could be associated with the Ba segregation as well. Ba grain boundary segregation has resulted in the lower grain boundary energy.[25] Furthermore, such grain boundary Ba segregation caused the diminishing of the grain boundaries with higher energy and promoted the steady-state distribution of those grain boundaries with lower energy and therefore enhanced crystal texture. This part of the finding on the effect of the grain boundary segregation on the crystal texture development is consistent with the literature[25,26] reporting that grain boundary segregation decreases the grain boundary energy in ceramics, and there is a strong inverse correlation between the relative energies of grain boundaries and the frequency with which they occur in microstructures and during microstructure evolution. In other words, the relatively higher-energy grain boundaries are more likely to be shrinking, while lower-energy interfaces are more likely to be growing that lead to a steady-state distribution of grain boundaries. In our case it is the development of strong texture along the $c$-axis.[27]

Overall, the present study demonstrates that non-stoichiometric Ba addition and Ba grain boundary segregation is very effective in lowering the carrier concentration and increasing the carrier mobility simultaneously. Moreover, the presence of heavy element Ba at grain boundaries enhances phonon scattering effect, so that the doped $Ca_3Ba_xCo_4O_{9+\delta}$ samples show suppressed $\kappa$. Eventually, TE performance of $Ca_3Ba_{0.05}Co_4O_{9+\delta}$ is prompted to $ZT$ value of 0.52 at 1073 K.

## CONCLUSIONS

A substantial enhancement of electrical transport properties was reached through Ba non-stoichiometric addition in the $Ca_3Co_4O_{9+\delta}$ system. For $Ca_3Ba_{0.05}Co_4O_{9+\delta}$, the simultaneous increases of $S$ and decrease of $\rho$ and $\kappa$ are achieved, resulting in high power factor of 843 $\mu W \cdot m^{-1} K^{-2}$ at 1007 K and high $ZT$ value of 0.52 at 1073 K. The nanostructure analysis reveal that, rather than forming the solid solution or substituting at Ca and/or Co sites in $Ca_3Co_4O_{9+\delta}$ crystal lattice, the added Ba segregates at $Ca_3Co_4O_{9+\delta}$ grain boundaries. Segregation of Ba and formation of a Ba-enriched grain boundary work effectively as a carrier filtering layer to decrease the carrier concentration and subsequently increase bulk Seebeck coefficient. Simultaneously, with optimized Ba addition, Ba grain boundary segregation also promotes the development of better crystal texture and thus increases the carrier mobility. The study opens the new directions and revolutionizes our ability to control the interface and grain boundaries for enhancing the TE properties of oxide ceramic.

## AUTHOR INFORMATION

### Corresponding Author

*Phone: +1 304 293 3269. Fax: +1 304 293 6689. E-mail: xueyan.song@mail.wvu.edu.

### Notes

The authors declare no competing financial interest.

## ACKNOWLEDGMENTS

P.C., C.B., and X.S. greatly appreciate the support from the National Science Foundation DMR (1254594).

## REFERENCES

(1) Masset, A. C.; Michel, C.; Maignan, A.; Hervieu, M.; Toulemonde, O.; Studer, F.; Raveau, B.; Hejtmanek, J. *Phys. Rev. B: Condens. Matter Mater. Phys.* **2000**, *62*, 166−175.
(2) Shikano, M.; Funahashi, R. *Appl. Phys. Lett.* **2003**, *82*, 1851−1853.
(3) Fergus, J. W. *J. Eur. Ceram. Soc.* **2012**, *32*, 525−540.
(4) Ohtaki, M. *J. Ceram. Soc. Jpn.* **2011**, *119*, 770−775.
(5) Koumoto, K.; Wang, Y.; Zhang, R.; Kosuga, A.; Funahashi, R. *Annu. Rev. Mater. Res.* **2010**, *40*, 363−394.
(6) Koumoto, K.; Funahashi, R.; Guilmeau, E.; Miyazaki, Y.; Weidenkaff, A.; Wang, Y. F.; Wan, C. L. *J. Am. Ceram. Soc.* **2013**, *96*, 1−23.
(7) Xu, G. J.; Funahashi, R.; Shikano, M.; Matsubara, I.; Zhou, Y. Q. *Appl. Phys. Lett.* **2002**, *80*, 3760−3762.



DOI: 10.1021/acs.inorgchem.5b01296
*Inorg. Chem.* 2015, 54, 9027−9032

(8) Prevel, M.; Perez, O.; Noudem, J. G. *Solid State Sci.* **2007**, *9*, 231−235.
(9) Wong-Ng, W.; Laws, W.; Talley, K. R.; Huang, Q.; Yan, Y.; Martin, J.; Kaduk, J. A. J. *J. Solid State Chem.* **2014**, *215*, 128−134.
(10) van Nong, N.; Pryds, N.; Linderoth, S.; Ohtaki, M. *Adv. Mater.* **2011**, *23*, 2484−2490.
(11) Katsuyama, S.; Takiguchi, Y.; Ito, M. *J. Mater. Sci.* **2008**, *43*, 3553−3559.
(12) Zhao, L.-D.; He, J.; Berardan, D.; Lin, Y.; Li, J.-F.; Nan, C.-W.; Dragoe, N. *Energy Environ. Sci.* **2014**, *7*, 2900−2924.
(13) Li, F.; Wei, T. R.; Kang, F. Y.; Li, J. F. *J. Alloys Compd.* **2014**, *614*, 394−400.
(14) Wu, T.; Tyson, T. A.; Bai, J.; Pandya, K.; Jaye, C.; Fischer, D. *J. Mater. Chem. C* **2013**, *1*, 4114−4121.
(15) Constantinescu, G.; Rasekh, S.; Torres, M. A.; Diez, J. C.; Madre, M. A.; Sotelo, A. *J. Alloys Compd.* **2013**, *577*, 511−515.
(16) Wu, N.; van Nong, N.; Pryds, N.; Linderoth, S. *J. Alloys Compd.* **2015**, *638*, 127−132.
(17) Wong-Ng, W.; Liu, G.; Martin, J.; Thomas, E. L.; Lowhorn, N.; Kaduk, J. A. *J. Appl. Phys.* **2010**, *107*, 033508.
(18) Constantinescu, G.; Madre, M. A.; Rasekh, S.; Torres, M. A.; Diez, J. C.; Sotelo, A. *Ceram. Int.* **2014**, *40*, 6255−6260.
(19) Liu, C. J.; Huang, L. C.; Wang, J. S. *Appl. Phys. Lett.* **2006**, *89*, 204102.
(20) Constantinescu, G.; Rasekh, S.; Torres, M. A.; Madre, M. A.; Sotelo, A.; Diez, J. C. *J. Mater. Sci.: Mater. Electron.* **2015**, *26*, 3466−3473.
(21) Song, X.; Chen, Y.; Chen, S.; Barbero, E.; Thomas, E. L.; Barnes, P. *Solid State Commun.* **2012**, *152*, 1509−1512.
(22) Bhaskar, A.; Huang, Y. C.; Liu, C. J. *Ceram. Int.* **2014**, *40*, 5937−5943.
(23) Song, X.; McIntyre, D.; Chen, X.; Barbero, E. J.; Chen, Y. *Ceram. Int.* **2015**, *41*, 11069−11074.
(24) Zide, J. M. O.; Vashaee, D.; Bian, Z. X.; Zeng, G.; Bowers, J. E.; Shakouri, A.; Gossard, A. C. *Phys. Rev. B: Condens. Matter Mater. Phys.* **2006**, *74*, 205335.
(25) Papillon, F.; Rohrer, G. S.; Wynblatt, P. *J. Am. Ceram. Soc.* **2009**, *92*, 3044−3051.
(26) Rohrer, G. S. *J. Am. Ceram. Soc.* **2011**, *94*, 633−646.
(27) Chen, S.; Song, X.; Chen, X.; Chen, Y.; Barbero, E. J.; Thomas, E. L.; Barnes, P. N. *J. Sol-Gel Sci. Technol.* **2012**, *64*, 627−636.



DOI: 10.1021/acs.inorgchem.5b01296
*Inorg. Chem.* 2015, 54, 9027−9032